Tiling Manifolds with Orthonormal Basis

Moo-Kyoung Chung, Anqi Qiu, Brendon Nacewicz, Seth Pollak, Richard Davidson

Tiling Manifolds with Orthonormal Basis

Moo K. Chung[1,2], Anqi Qiu[4], Brendon, M. Nacewicz[2],
Seth Pollak[3], Richard J. Davidson[2,3]

[1]Department of Biostatistics and Medical Informatics,
[2]Waisman Laboratory for Brain Imaging and Behavior,
[3] Department of Psychology and Psychiatry
University of Wisconsin, Madison, USA
[4]Division of Bioengineering, Faculty of Engineering
National University of Singapore, Singapore
mkchung@wisc.edu

Abstract. One main obstacle in building a sophisticated parametric model along an arbitary anatomical manifold is the lack of an easily available orthonormal basis. Although there are at least two numerical techniques available for constructing an orhonormal basis such as the Laplacian eigenfunction approach and the Gram-Smidth orthogonalization, they are computationally not so trivial and costly. We present a relatively simpler method for constructing an orthonormal basis for an arbitrary anatomical manifold. On a unit sphere, a natural orthonormal basis is the spherical harmonics which can be easily computed. Assuming the manifold is topologically equivalent to the sphere, we can establish a smooth mapping ζ from the manifold to the sphere. Such mapping can be obtained from various surface flattening techniques. If we project the spherical harmonics to the manifold, they are no longer orthonormal. However, we claim that there exists an orthonormal basis that is the function of spherical harmonics and the spherical mapping ζ.
The detailed step by step procedures for the construction is given along with the numerical validation using amygdala surfaces as an illustration. As an application, we propose the pullback representation that reconstructs surfaces using the orthonormal basis obtained from an average template. The pullback representation introduces less inter-subject variability and thus requires far less number of coefficients than the traditional spherical harmonic representation. The source code used in the study is freely available at
http://www.stat.wisc.edu/∼mchung/research/amygdala.

1 Introduction

We present a novel orthonormal basis construction method for an arbitrary anatomical surface that is topologically equivalent to a sphere. The method avoids the well known Gram-Smidth orthogonalization procedure [7], which is inefficient for high resolution polygonal meshes. In order to perform the Gram-Smidth orthogonalization as described in [7], for a surface mesh with n vertices,

we need to perform the Choleski decomposition as well as the inversion of matrix of size $n \times n$. For a cortical mesh generated with FreeSurfer [6], n can easily reach up to 200000.

On the other hand, Qiu et al. [15] constructed an orthonormal basis as the eigenfunctions of the Laplace-Beltrami operator in a bounded regions of interest (ROI) on a cortical surface (Figure 3). The finite element method (FEM) is used to numerically construct the orthonormal basis by solving a system of large linear equations. The weakness of the FEM approach is the computational burden of inverting a matrix of size $n \times n$. One advantage of the eigenfunction approach is that since the eigenfunctions and eigenvalues are directly related to the Laplace-Beltrami operator, it is trivial and geometrically intuitive to construct the heat kernel analytically and perform a various heat kernel smoothing based modeling [4].

We propose a completely different method that avoids the computational bottleneck by using a conceptually different machinery. We assume an arbitrary anatomical surface to be topologically equivalent to a sphere. Then using a smooth mapping ζ obtained from a surface flattening technique, we project the spherical harmonics to the anatomical surface. Obviously the projected spherical harmonics will no longer be orthonormal. However, if we correct the metric distortion introduced from the surface flattening, we may able to make the projected spherical harmonics orthonormal somehow. This is the basic idea behind our new proposed method. For the surface flattening, we present a new method that treats the mapping ζ as the geodesic path of the heat equilibrium state.

As an application of the proposed technique, we present the novel *pullback representation* for parameterizing anatomical boundaries that outperforms the traditional spherical harmonic (SPHARM) representation [2] [3] [8] [16] [17]. We claim that our proposed representation has far less intersubject variability in the estimated parameters than SPHARM and converges faster to the true boundary with less number of basis.

2 Methods

It is assumed that the anatomical boundary $\mathcal{M}$ is a smooth 2-dimensional Riemannian manifold parameterized by two parameters. The one-to-one mapping ζ from point $\mathbf{p} = (p_1, p_2, p_3)' \in \mathcal{M}$ to $\mathbf{u} = (u_1, u_2, u_3)' \in S^2$, a unit sphere, can be obtained from various surface flattening techniques such as conformal mapping [1] [8] [9], quasi-isometric mapping [18], area preserving mapping [2] [16] [17] and the deformable surface algorithm [13]. Since the conformal mapping tend to introduce huge area distortion, most spherical harmonic literature tend to use area preserving mapping [2] [16] [17].

In this paper, we present a new flattening technique via the geodesic trajectory of the equilibrium sate of heat diffusion. The proposed flattening technique is numerically simpler than any other available methods and does not require optimizing a cost function. The methodology is illustrated using the 47 amyg-

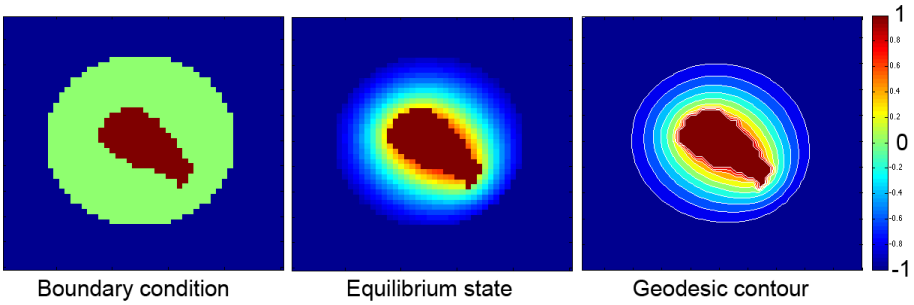

Fig. 1. The diffusion equation with a heat source (amygdala) and a heat sink (enclosing sphere) corresponds. After sufficient amount of diffusion, the heat equilibrium state is reached. By tracing the geodesic path from the heat source to the heat sink using the geodesic contours, we obtain a smooth mapping ζ.

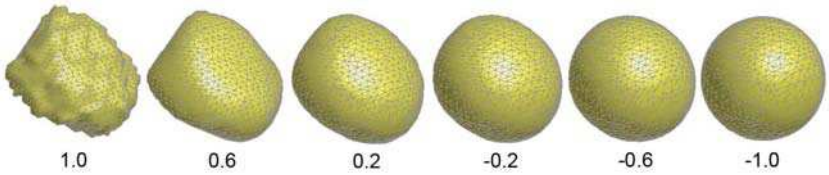

Fig. 2. Amygala surface flattening is done by tracing the geodesic path of the heat equilibrium state. The numbers corresponds to the different the geodesic contours. For simple shapes like amygde, 5 to 10 contours are sufficient for tracing the geodesic path.

dala binary segmentation obtained from the 3-Tesla magnetic resonance images (MRI).

High resolution anatomical MRI were obtained using a 3-Tesla GE SIGNA scanner with a quadrature head coil. Details on image acquisition parameters are given in [14]. MRIs are reoriented to the pathological plane for optimal segmentation and comparison with an atlas. This global alignment guarantee that amygdala are approximately aligned in the same orientation.

Manual amygdala segmentation was done by a trained expert and the reliability of the manual segmentation was validated by two raters on 10 amygdale resulting in interclass correlation of 0.95 and the intersection over the union of 0.84 [14]. Afterwards a marching cubes algorithm was used to extract the boundary of the binary segmentation as a triangle mesh with approximately 2000-3000 vertices. The amygdala surface is then mapped onto a sphere using the new flattening algorithm.

2.1 Diffusion-Based Surface Flattening

Given an amygdala binary segmentation $\mathcal{M}_a$, we put a larger sphere $\mathcal{M}_s$ that encloses the amygala (Figure 1 left). The amygdala and sphere serve as Dirichlet boundary conditions for solving the Laplace equation. The amygdala is assigned the value 1 while the enclosing sphere is assigned the value -1, i.e.

$$f(\mathcal{M}_a, \sigma) = 1, f(\mathcal{M}_s, \sigma) = -1 \tag{1}$$

for all σ. The amygdala and the sphere serve as a heat source and a heat sink respectively. Then we solve an isotropic diffusion

$$\frac{\partial f}{\partial \sigma} = \Delta f \tag{2}$$

within the empty space bounded by the amygdala and the sphere. Δ is the 3D Laplacian. After enough diffusion, the system reaches the heat equilibrium state where the additional diffusion does not make any difference in the heat distribution (Figure 1 middle). Once we obtained the equilibrium state, we trace the geodesic path from the heat source to the heat sink for every mesh vertices. The trajectory of the geodesic path provides a smooth mapping from the amygdala surface to the sphere. The geodesic path can be easily traced by constructing geodesic contours that correspond to the level set of the equilibrium state (Figure 1 right). Then the geodesic path is constructed by finding the shortest distance from one contour to the next and iteratively connecting the path together. Figure 2 shows the process of flattening using five contours corresponding to the temperature 0.6, 0.2, -0.2, -0.6, -1.0.

Although we did not apply our flattening technique to other anatomical objects, the proposed method can be applied to more complex object than the amygdala. At the equilibrium state, we no longer has change in heat change over time, i.e. $\frac{\partial f}{\partial \sigma} = 0$, so we have the Laplace equation

$$\Delta f = 0$$

with the same boundary condition. The Laplace equation has been previously used to trace the distance between outer and inner cortical surfaces and to compute cortical thickness [10] [12] [19]. Since the solution to the Laplace equation with the boundary condition (1) is unique even for highly convoluted and folded structures, the geodesic path will be uniquely defined.

2.2 Orhonormal basis in two sphere S^2

Suppose a unit sphere S^2 is represented as a high resolution triangle mesh consisting of the vertex set $\mathcal{V}(S^2)$. We have used an almost uniformly sampled mesh with 2562 vertices and 5120 faces. Let us parameterize coordinates $\mathbf{u} \in S^2$ with parameters θ, φ:

$$(u_1, u_2, u_3) = (\sin\theta\cos\varphi, \sin\theta\sin\varphi, \cos\theta),$$

where $(\theta, \varphi) \in \mathcal{N} = [0, \pi] \otimes [0, 2\pi)$. The polar angle θ is the angle from the north pole and φ is the azimuthal angle. The orthonormal basis on the unit sphere is given by the eigenfunctions of

$$\Delta f + \lambda f = 0,$$

where Δ is the spherical Laplacian. The eigenfunction Y_{lm} corresponding to the eigenvalue $l(l+1)$ is called the spherical harmonic of degree l and order m [5]. With respect to the inner product

$$\langle f, g \rangle_{S^2} = \int_{S^2} f(\mathbf{u}) g(\mathbf{u}) \, d\mu(\mathbf{u}), \tag{3}$$

with measure $d\mu(\mathbf{u}) = \sin\theta d\theta d\varphi$, Y_{lm} form the orthonormal basis in $L^2(S^2)$, the space of square integrable functions on S^2, i.e.

$$\langle Y_{lm}, Y_{l'm'} \rangle_{S^2} = \delta_{ll'} \delta_{mm'}. \tag{4}$$

The inner product can be numerically computed as the Riemann sum over mesh vertices as

$$\langle Y_{lm}, Y_{l'm'} \rangle_{S^2} \approx \sum_{\mathbf{u}_j \in \mathcal{V}(S^2)} Y_{lm}(\mathbf{u}_j) Y_{l'm'}(\mathbf{u}_j) D_{S^2}(\mathbf{u}_j), \tag{5}$$

where $D_{S^2}(\mathbf{u}_j)$ is the discrete approximation of $d\mu(\mathbf{u})$. Let $T^1_{\mathbf{u}_j}, T^2_{\mathbf{u}_j}, \cdots, T^{j_m}_{\mathbf{u}_j}$ be the area of triangles containing the vertex $\mathbf{u}_j$. Then we estimate $D_{S^2}(\mathbf{u}_j)$ as

$$D_{S^2}(\mathbf{u}_j) = \frac{1}{3} \sum_{k=1}^{j_m} T^k_{\mathbf{u}_j}. \tag{6}$$

The discrete approximation (6) defines the area of triangles at a mesh vertex. The factor $1/3$ is chosen in such a way that

$$\sum_{\mathbf{u}_j \in \mathcal{V}(S^2)} D_{S^2}(\mathbf{u}_j) = 12.5514 = 4 \cdot 3.1378,$$

analogous to the relationship

$$\int_{S^2} d\mu(\mathbf{p}) = 4\pi.$$

The discrepancy between the integral and its discrete counter part is due to the mesh resolution and it should become smaller as the mesh resolution increases.

Based on the proposed discretization scheme, we have computed the inner product (5) for all degrees $0 \leq l, l' \leq 20$. Figure 3 (left) shows the inner products for every possible pairs. Since for up to the k-th degree, there are total $(k+1)^2$ basis functions, we have total 441^2 possible inner product pairs, which is displayed as a matrix. For the diagonal terms, we obtained 0.9988 ± 0.0017 while for the off-diagonal terms, we have obtained 0.0000 ± 0.0005 indicating our basis and the discretization scheme is orthonormal with two decimal accuracy.

2.3 Orthonormal basis on manifold $\mathcal{M}$

For $f, g \in L^2(\mathcal{M})$, the orthonormality is defined with respect to the inner product

$$\langle f, g \rangle_{\mathcal{M}} = \int_{\mathcal{M}} f(\mathbf{p}) g(\mathbf{p}) \, d\mu(\mathbf{p}).$$

Using the spherical harmonics in S^2, it is possible to construct an orthonormal basis in $\mathcal{M}$ numerically without the computational burden of solving the large matrix inversion associated with the eigenfunction method or the Gram-Smidth orthogonalization. Since the spherical harmonics are orthonormal in S^2 and, the manifolds S^2 and $\mathcal{M}$ can be deformed to each other by the mapping ζ, one would guess that the orthonormal basis in $\mathcal{M}$ can be obtained somehow using the spherical harmonics. Surprisingly this guess is not wrong as we will show in this section.

For $f \in L^2(S^2)$, let us define the *pullback operation* * as

$$\zeta^* f = f \circ \zeta.$$

While f is defined on S^2, the pullbacked function $\zeta^* f$ is defined on $\mathcal{M}$. The schematic of the pull back operation is given in Figure 6 (a). Then even though we do not have orthonormality on the pullbacked spherical harmonics, i.e.,

$$\langle \zeta^* Y_{lm}, \zeta^* Y_{l'm'} \rangle_{\mathcal{M}} \neq \delta_{ll'} \delta_{mm'},$$

we can make them orthonormal by using the Jacobian determinant of the mapping ζ somehow.

Consider the Jacobian J_ζ of the mapping $\zeta : \mathbf{p} \in \mathcal{M} \to \mathbf{u} \in S^2$ defined as

$$J_\zeta = \frac{\partial \mathbf{u}(\theta, \varphi)}{\partial \mathbf{p}(\theta, \varphi)}.$$

For functions $f, g \in L^2(S^2)$, we have the following change of variable relationship:

$$\langle f, g \rangle_{S^2} = \int_{\mathcal{M}} \zeta^* f(\mathbf{p}) \zeta^* g(\mathbf{p}) |\det J_\zeta| \, d\mu(\mathbf{p}). \tag{7}$$

Similarly we have the inverse relationship given as

$$\langle \zeta^* f, \zeta^* g \rangle_{\mathcal{M}} = \int_{S^2} f(\mathbf{u}) g(\mathbf{u}) |\det J_{\zeta^{-1}}| \, d\mu(\mathbf{u}). \tag{8}$$

By letting $f = Y_{lm}$ and $g = Y_{l'm'}$ in (7), we obtain

$$\delta_{ll'} \delta_{mm'} = \int_{\mathcal{M}} \zeta^* Y_{lm} \zeta^* Y_{l'm'} |\det J_\zeta| \, d\mu(\mathbf{p}) \tag{9}$$

Equation (9) demonstrates that functions

$$Z_{lm} = |\det J_\zeta|^{1/2} \zeta^* Y_{lm} \tag{10}$$

are orthonormal in $\mathcal{M}$. We will refer l as degree and m as order of the basis function. Using the Riesz-Fischer theorem [11], it is not hard to show that Z_{lm} form a complete basis in $L^2(\mathcal{M})$.

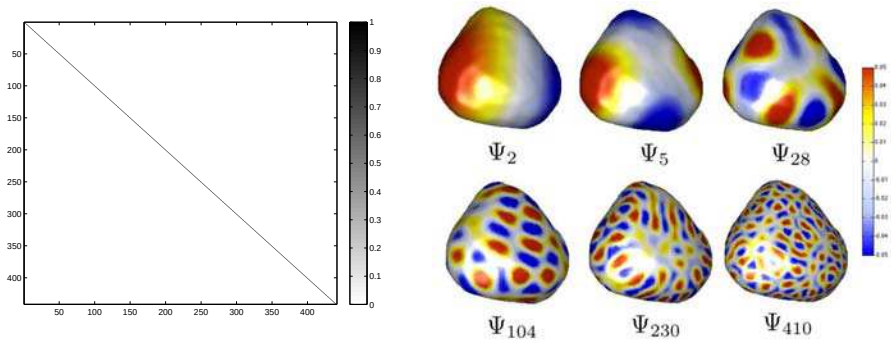

Fig. 3. Left: inner products of eigenfunctions of the Laplacian for every pairs [15]. The pairs are rearranged from low to high degree. Right: representative eigenfunctions Ψ_j on the left amygdala template surface obtained by solving $\Delta\Psi_j + \lambda_j\Psi_j = 0$.

2.4 Numerical Implementation

Although the expression (10) provides a nice analytical form for an orthonormal basis for an arbitrary manifold $\mathcal{M}$, it is not practical. If one want to use the basis (10), the Jacobian determinant needs to be numerically estimated somehow. We present a new discrete estimation technique for the surface Jacobian determinant that avoids estimating unstable spatial derivative estimation.

The Jacobian determinant J_ζ of the mapping ζ can be expressed in terms of the Riemannian metric tensors associated with the manifolds S^2 and $\mathcal{M}$. Consider determinants $\det g_{S^2}$ and $\det g_{\mathcal{M}}$ of the Riemannian metric tensors associated with the parameterizations $\mathbf{u}(\theta,\varphi)$ and $\mathbf{p}(\theta,\varphi)$ respectively. Note that the integral of the area elements $\sqrt{\det g_{S^2}}$ and $\sqrt{\det g_{\mathcal{M}}}$ with respect to the parameter space $\mathcal{N}$ gives the total area of the manifolds, i.e.

$$\int_{\mathcal{N}} \sqrt{\det g_{S^2}}\, d\mu(\theta,\varphi) = 4\pi, \quad \int_{\mathcal{N}} \sqrt{\det g_{\mathcal{M}}}\, d\mu(\theta,\varphi) = \mu(\mathcal{M}).$$

Then we have the relationship

$$|\det J_{\zeta^{-1}}| = \frac{\sqrt{\det g_{\mathcal{M}}}}{\sqrt{\det g_{S^2}}}, \quad |\det J_\zeta| = \frac{\sqrt{\det g_{S^2}}}{\sqrt{\det g_{\mathcal{M}}}}.$$

Note that the Jacobian determinant $\det J_\zeta$ measures the amount of contraction or expansion in the mapping ζ from $\mathcal{M}$ to S^2. So it is intuitive to have this quantity to be expressed as the ratio of the area elements. Consequently the discrete estimation of the Jacobian determinant at mesh vertex $\mathbf{u}_j = \zeta(\mathbf{p}_j)$ is obtained as

$$|\det J_\zeta| \approx \frac{D_{S^2}(\mathbf{u}_j)}{D_{\mathcal{M}}(\mathbf{p}_j)}.$$

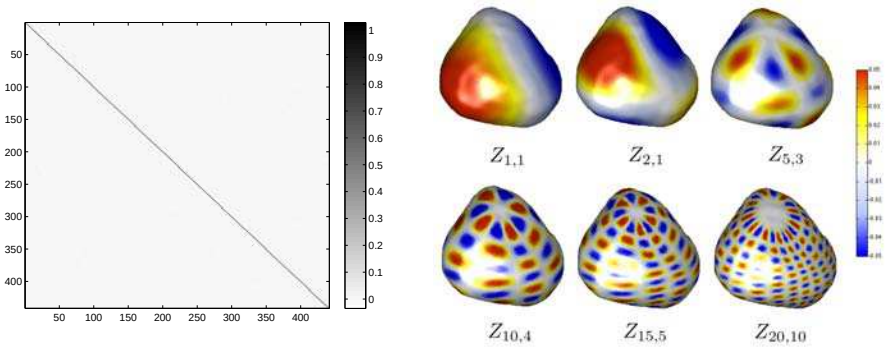

Fig. 4. Left: inner products of spherical harmonics computed using formula (3) for every pairs. The pairs are rearranged from low to high degree and order. There are total $(20+1)^2 = 441$ possible pairs for up to degree 20. Right: representative orthonormal basis Z_{lm} on the left amygdala template surface.

Then our orthonormal basis is given by

$$Z_{lm}(\mathbf{p}_j) = \sqrt{\frac{D_{S^2}(\zeta(\mathbf{p}_j))}{D_{\mathcal{M}}(\mathbf{p}_j)}}\zeta^* Y_{lm}(\mathbf{p}_j). \tag{11}$$

The numerical accuracy can be determined by computing the inner product

$$\begin{aligned}
\langle Z_{lm}, Z_{l'm'}\rangle_{\mathcal{M}} &\approx \sum_{\mathbf{p}_j \in \mathcal{V}(\mathcal{M})} Z_{lm}(\mathbf{p}_j) Z_{lm}(\mathbf{p}_j) D_{\mathcal{M}}(\mathbf{p}_j). \\
&= \sum_{\mathbf{p}_j \in \mathcal{V}(\mathcal{M})} \zeta^* Y_{lm}(\mathbf{p}_j) \zeta^* Y_{l'm'}(\mathbf{p}_j) D_{S^2}(\zeta(\mathbf{p}_j)) \\
&= \sum_{\mathbf{u}_j \in \mathcal{V}(S^2)} Y_{lm}(\mathbf{u}_j) Y_{l'm'}(\mathbf{u}_j) D_{S^2}(\mathbf{u}_j) \\
&= \langle Y_{lm}, Y_{l'm'}\rangle_{S^2}
\end{aligned}$$

Since this is tautology, the order of the numerical accuracy in Z_{lm} is identical to that of spherical harmonics given in the previous section. There is no need for additional validation other than given in the previous section. Hence we conclude that our basis is in fact orthonormal within two decimal accuracy. Figure 4 shows the result of our numerical procedure applied to the average amygdala surface template. The template surface is constructed by averaging the surface using the spherical harmonic correspondence given in [3].

We have also constructed an orthonormal basis on a cortical surface with more than 40000 mesh vertices (Figure 5). The diagonal elements in the inner product matrix are 0.9999 ± 0.0001 indicating that our basis is orthonormal within three decimal accuracy. As the mesh resolution increases, we expect to have increased accuracy. The proposed orthonormal basis construction methods

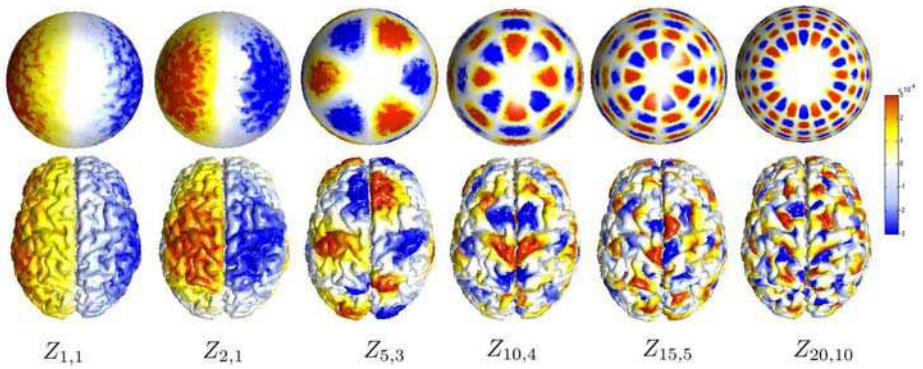

Fig. 5. Orthonormal basis Z_{lm} on a cortical surface. The basis is projected on a sphere to show how the nonuniformity of the Jacobian determinant is effecting the spherical harmonics Y_{lm}. The color scale is thresholded at ± 0.003 for better visualization.

avoids inverting matrix of size larger than 40000×40000 associated with the eigenfunction approach and the Gram-Smidth orthogonalization process.

Although the pattern of tiling in the eigenfunction approach (Figure 3) and the pullback based method (Figure 4) looks different, it can be shown that they are actually linearly dependent.

3 Application: Pullback Representation

As an application of the proposed orthonormal basis construction, we present a new variance reducing Fourier Series representation that outperforms the traditional spherical harmonic representation [2] [3] [8] [16] [17]. We will call this method as the *pullback representation*.

The spherical harmonic (SPHARM) representation models the surface coordinates with respect to a unit sphere as

$$\mathbf{p}(\theta, \varphi) = \sum_{l=0}^{k} \sum_{m=-l}^{l} \mathbf{p}_{lm}^0 Y_{lm}(\theta, \varphi) \tag{12}$$

where $\mathbf{p}_{lm}^0 = \langle \mathbf{p}, Y_{lm} \rangle_{S^2}$ are spherical harmonic coefficients, which can be viewed as random variables. The coefficients are estimated using the *iterative residual fitting algorithm* [3] that breaks a larger least squares problem into smaller ones in an iterative fashion. The MATLAB code for performing the iterative residual fitting algorithm for arbitrary surface mesh is given in http://www.stat.wisc.edu/~mchung/softwares/weighted-SPHARM/weighted-SPHARM.hmtl. Note that all MRIs were reoriented to the pathological plane guaranteeing an approximate global alignment before the surface flattening to increase the robustness of the coefficient estimation.

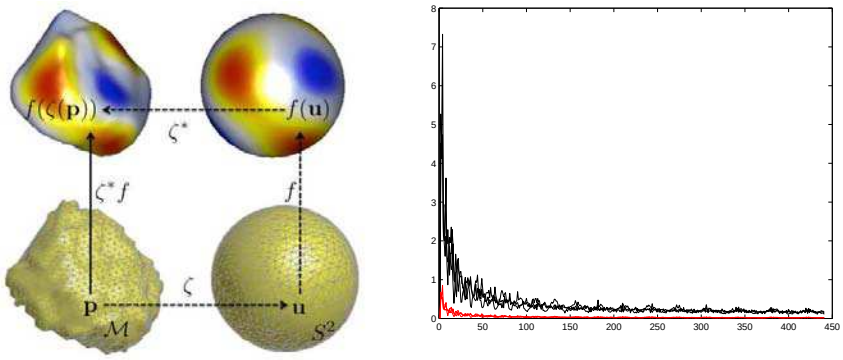

Fig. 6. Left: schematic showing how the pullback operation * is working. Point $\mathbf{p} \in \mathcal{M}$ is mapped to $\mathbf{u} \in S^2$ via our new flattening technique. As an illustration $f = Y_{3,2} + 0.6Y_{2,1}$ is plotted on S^2. The function f is pulled back onto $\mathcal{M}$ by ζ. Right: sample standard deviation of Fourier coefficients of for 47 subjects plotted over the index of basis. In average, the traditional SPHARM representation (black) has 88% more variability than the pull back method (red).

The shortcoming of the spherical harmonic representation is that the reconstruction is respect to a unit sphere that is not geometrically related to the original anatomical surface. On the other hand, the pullback representation will reconstruct the surface with respect to the average template surface reducing substantial amount of variability compared to SPHARM.

In the pullback representation, we represent the surface coordinates with respect to the template surface $\mathcal{M}$ as

$$\mathbf{p}(\theta, \varphi) = \sum_{l=0}^{k} \sum_{m=-l}^{l} \mathbf{p}_{lm}^1 Z_{lm}(\theta, \varphi) \tag{13}$$

with $\mathbf{p}_{lm}^1 = \langle \mathbf{p}, Z_{lm} \rangle_{\mathcal{M}}$. Then we claim that the pullback representation has smaller variance in the estimated coefficients so that

$$\mathrm{Var}(\mathbf{p}_{lm}^1) \leq \mathrm{Var}(\mathbf{p}_{lm}^0). \tag{14}$$

The equality in (14) is obtained when the template $\mathcal{M}$ becomes the unit sphere, in which case the spherical mapping ζ collapses to the identity, and the inner products coincide. We have computed the sample standard deviation of Fourier coefficients for 47 subjects using the both representations. In average, the SPHARM contains 88% more intersubject variability compared to the pullback representation (Figure 6 right). This implies that SPHARM is an inefficient representation and requires more number of basis to represent surfaces compared to the pullback method.

Although the pullback method is more efficient, the both representations (12) and (13) converge to each other as k goes to infinity. We have computed the

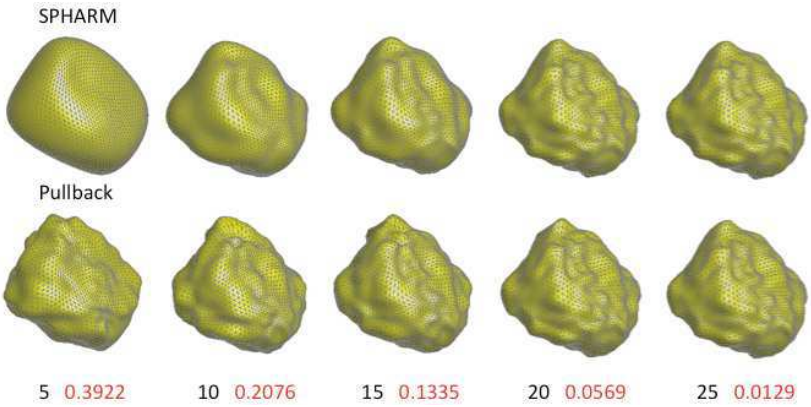

Fig. 7. Comparison of SPHARM and the pullback representations for degree 5 to 25. Red colored numbers are the average Euclidean distance between two representations in mm.

squared Euclidean distance between two representations numerically (Figure 7). In average, the difference is 0.0569 mm for 20 degree representation negligible for 1mm resolution MR. Figure 7 also visually demonstrate that the pullback representation converges to the true manifold faster than SPHARM again showing the inefficiency of the SPHARM representation.

4 Conclusion

We have introduced a computationally efficient way to construct an approximate orthonormal basis on an arbitrary manifold by pulling back the spherical harmonics to the manifold and accounting for the metric distortion using the Jacobian determinant. The proposed technique is very general so that it can be applicable to other types of anatomical manifolds. The constructed basis on an amygdala is used to show the new pullback representation that reconstruct the manifold as linear combination of the basis functions.

References

1. S. Angenent, S. Hacker, A. Tannenbaum, and R. Kikinis. On the laplace-beltrami operator and brain surface flattening. *IEEE Transactions on Medical Imaging*, 18:700–711, 1999.
2. C. Brechbuhler, G. Gerig, and O. Kubler. Parametrization of closed surfaces for 3d shape description. *Computer Vision and Image Understanding*, 61:154–170, 1995.
3. M.K. Chung, L. Shen Dalton, K.M., A.C. Evans, and R.J. Davidson. Weighted fourier representation and its application to quantifying the amount of gray matter. *IEEE Transactions on Medical Imaging*, 26:566–581, 2007.

4. M.K. Chung, S. Robbins, Davidson R.J. Alexander A.L. Dalton, K.M., and A.C. Evans. Cortical thickness analysis in autism with heat kernel smoothing. *NeuroImage*, 25:1256–1265, 2005.
5. R. Courant and D. Hilbert. *Methods of Mathematical Physics: Volume II*. Interscience, New York, english edition, 1953.
6. B. Fischl and A.M. Dale. Measuring the thickness of the human cerebral cortex from magnetic resonance images. *PNAS*, 97:11050–11055, 2000.
7. K.M. Gorski. On determining the spectrum of primordial inhomogeneity from the cobe dmr sky maps: I. method. *Astrophysical Journal, 430*, 430:L85, 1994.
8. X. Gu, Y.L. Wang, T.F. Chan, T.M. Thompson, and S.T. Yau. Genus zero surface conformal mapping and its application to brain surface mapping. *IEEE Transactions on Medical Imaging*, 23:1–10, 2004.
9. M. K. Hurdal and K. Stephenson. Cortical cartography using the discrete conformal approach of circle packings. *NeuroImage*, 23:S119S128, 2004.
10. S.E. Jones, B.R. Buchbinder, and I. Aharon. Three-dimensional mapping of cortical thickness using laplace's equation. *Human Brain Mapping*, 11:12–32, 2000.
11. A.N. Kolmogorov and S.V. Fomin. Introductory real analysis. Dover Publications, Inc, New York, 1970.
12. J. P. Lerch and A.C. Evans. Cortical thickness analysis examined through power analysis and a population simulation. *NeuroImage*, 24:163–173, 2005.
13. J.D. MacDonald, N. Kabani, D. Avis, and A.C. Evans. Automated 3-D extraction of inner and outer surfaces of cerebral cortex from mri. *NeuroImage*, 12:340–356, 2000.
14. B.M. Nacewicz, K.M. Dalton, T. Johnstone, M.T. Long, E.M. McAuliff, T.R. Oakes, A.L Alexander, and R.J. Davidson. Amygdala volume and nonverbal social impairment in adolescent and adult males with autism. *Arch. Gen. Psychiatry*, 63:1417–1428, 2006.
15. A. Qiu, D. Bitouk, and M.I. Miller. Smooth functional and structural maps on the neocortex via orthonormal bases of the laplace-beltrami operator. *IEEE Transactions on Medical Imaging*, 25:1296–1396, 2006.
16. L. Shen, J. Ford, F. Makedon, and A. Saykin. surface-based approach for classification of 3d neuroanatomical structures. *Intelligent Data Analysis*, 8:519–542, 2004.
17. M. Styner, I. Oguz, S. Xu, C. Brechbuhler, D. Pantazis, J. Levitt, M. Shenton, and G. Gerig. Framework for the statistical shape analysis of brain structures using spharm-pdm. In *Insight Journal, Special Edition on the Open Science Workshop at MICCAI*, 2006.
18. B. Timsari and R. Leahy. An optimization method for creating semi-isometric flat maps of the cerebral cortex. In *The Proceedings of SPIE, Medical Imaging*, 2000.
19. A. Yezzi and J.L. Prince. An eulerian pde approach for computing tissue thickness. *IEEE Transactions on Medical Imaging*, 22:1332–1339, 2003.